Size effects in microstructured superconductors and quantum materials

Fermin, R.

5

MESOSCOPIC SUPERCONDUCTING MEMORY ELEMENTS BASED ON BISTABLE MAGNETIC TEXTURES

R. Fermin, N. Scheinowitz, J. Aarts & K. Lahabi

With the ever-increasing energy need to process big data, the realization of low-power computing technologies, such as superconducting logic and memories, has become a pressing issue. Developing fast and non-volatile superconducting memory elements, however, remains a challenge. Superconductor-ferromagnet hybrid devices, like the ones presented in Chapter 4, offer a promising solution, as they combine ultra-fast manipulation of spins with dissipationless readout. In this chapter, we present a new type of non-volatile Josephson junction memory that utilizes the bistable magnetic texture of a single mesoscopic ferromagnet. We use micromagnetic simulations to design an ellipse-shaped planar junction structured from an Nb/Co bilayer. The ellipse can be prepared as uniformly magnetized or as a pair of vortices at zero applied field. The two states yield considerably different critical currents, enabling reliable electrical readout of the element. We describe the mechanism used to control the critical current by applying numerical calculations to quantify the local stray field from the ferromagnet, which shifts the superconducting interference pattern. Our approach presents a novel route towards realizing superconducting memory applications by combining micromagnetic modeling with bistable spin-textured junctions.

This chapter is based on the paper published in *Phys. Rev. Res.* **4**, 033136 (2022).

5.1. INTRODUCTION

In recent years, energy-hungry data centers have accounted for more than 1% of the global electricity consumption, which is projected to increase to 3-13% by 2030[1]. As data centers are responsible for 0.3% of the overall carbon emissions, the development of low-power supercomputers has become an immediate global concern[2]. Due to their non-dissipative nature, superconducting logic and memory devices present a tantalizing route to address this issue, promising enormous savings, even accounting for cryogenic cooling[3–7]. While several classes of high-performance superconducting processors already exist, cryogenic memories remain relatively underdeveloped. Non-volatility and scalability, in particular, have been the major obstacles in the industrial realization of superconducting memories.

The combination of superconducting and ferromagnetic elements can tackle the non-volatility issue through S−F−S devices, in which different (stable) magnetic configurations yield different critical supercurrents. Much work has been done on stacked magnetic Josephson junctions with a weak ferromagnetic barrier, where small magnetic field pulses could switch the critical current. [8–11] However, the weak ferromagnet used in such systems has a typically low Curie temperature (around 10 K), limiting their non-volatility. Josephson memories have also been extensively studied in so-called pseudo-spin-valve (S−F−N−F′−S) devices, where the magnetization of two ferromagnetic layers, separated by a normal metal, could be set parallel or antiparallel to yield a change in critical current. [12–18] The work on pseudo-spin-valves has also been extended to multilayer Josephson devices featuring triplet supercurrents, which not only carry charge but also spin. [19, 20] Finally, all-oxide devices, which can operate at high temperatures, were recently examined. [21] In general, the existing non-volatile Josephson memories utilize an intricate layer set and face several obstacles, such as interlayer coupling between magnetic layers and stochastic distribution of magnetic flux in the junction. Other problems include insufficient contrast between states for electrical readout, and the requirement for applying a large writing field.

In this chapter, we address these challenges and present an alternative route for developing non-volatile Josephson memory elements, where information is stored by the spin texture of a single mesoscopic ferromagnet. Magnetic textures, in general, and specifically ferromagnetic vortices, can be manipulated by applying pulsed microwave radiation, leading to the realization of ultra-fast electronics[22–24]. Combining information inscription in spin textures with the non-dissipative nature of supercurrents can thus lead to the realization of high-speed, low-power, and non-volatile memory elements. Furthermore, the synergy between superconductivity and magnetic textures is amplified further by allowing for triplet supercurrents, paving the road for superconducting spintronics[25–27]. Textured S−F-hybrid devices open a new paradigm in superconducting memory applications.

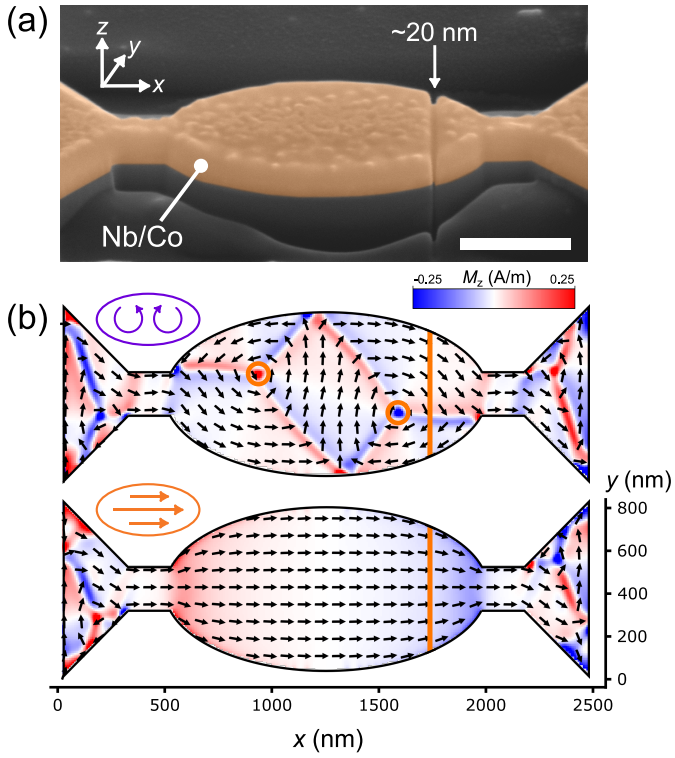

Figure 5.1: (a) False colored scanning electron micrograph of the ellipse-shaped S−F−S junction device A. The Co weak link is formed by the indicated trench (∽20 nm in size) that separates the two Nb electrodes. The scale bar corresponds to 500 nm. (b) Shows the simulated bistable spin textures at zero field. The cobalt is either magnetized along the long axis of the device (M-state) or hosts two stable vortices (V-state). Orange circles highlight the vortex cores, and the orange line indicates the trench location. The color scale indicates the out-of-plane magnetization of the top of the cobalt layer.

Here we show the realization of a micrometer-sized superconducting memory element based on bistable spin textures in the F-layer of elliptical versions of the S−F−S Josephson junctions presented in Chapter 4. By combining micromagnetic simulations with nanostructured hybrid devices, we are able to control the transport behavior of our devices with their magnetic texture. By applying a magnetic field of 40 mT as the writing operation, we can reliably switch between two stable spin textures: one is uniformly magnetized, and the other hosts a pair of ferromagnetic vortices. These correspond to minimum and maximum critical supercurrent of the junction, respectively. We obtain a factor of five difference in the critical current between the two states, which allows for a facile and reliable electrical readout of the element. By quantifying the local stray field from the ferromagnet, we show that the difference in critical current is caused by a shift in the superconducting interference pattern. Moreover, the magnetic bistability enables us to use writing fields that are considerably smaller than the local stray field from the ferromagnet. We confirm the memory is stable, non-volatile, and non-destructive upon readout.

5.2. ELLIPSE-SHAPED S–F–S JUNCTIONS

Using the procedure described in Chapter 3, we prepare elliptical S–F–S junctions from a cobalt (65 nm) niobium (50 nm) bilayer (deposited in an ultra-high vacuum by Ar-sputtering). Figure 5.1a shows a false-colored scanning electron micrograph of such an ellipse device, having dimensions of 1500 nm by 750 nm (long and short axes, respectively). Micromagnetic simulations show that the zero-field spin texture of such devices is expected to be bistable: either the cobalt layer is magnetized along the long axis of the ellipse (we call this the M-state) or two ferromagnetic vortices are stable near each focal point of the ellipse (V-state). We depict simulation results from these states in Figure 5.1b. The full technical details of the simulations are presented in Appendix A. Essentially, this allows for writing a bit with the value "0" (M-state) or "1" (V-state) into the spin texture of the device. We prepare the states by first applying a 40 mT in-plane field either parallel to the long or short axis of the devices. Next, after removing the field along the short (long) axis, the V-state (M-state) is stable in the device.

The trench is positioned near the focal point of the ellipse, which corresponds to the approximate location of a vortex core in the V-state. As discussed later, this particular location is designed to optimize the stray field-driven mechanism used to assign different critical currents to the M- and V-states. In this chapter, we describe two of these elliptical devices (devices A and B), although all observations are repeated for a large number of samples. Figure 5.2 shows the resistance versus temperature of device A, measured with a current of 20 μA. If the sample is prepared in the V-state, we find two transitions. The first corresponds to the bulk superconducting critical temperature of the Nb layer, the second is due to the superconducting proximity effect in the S–F–S junction formed by the trench. In contrast, the M-state does not show a second tran-

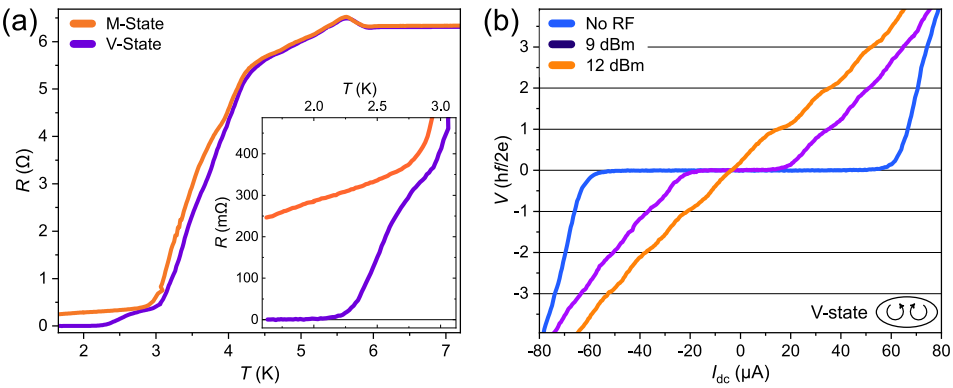

Figure 5.2: Basic transport characteristics of device A. In (a) we show the resistance versus temperature curves for both the M- and V-state, measured using 20 μA current bias. The critical current is suppressed below 20 μA in the M-state. The inset shows the low-temperature behavior. (b) depicts three IV-characteristics of the sample in the V-state, acquired under different RF radiation powers. The frequency is 1.6 GHz, and the temperature is 1.6 K. The measured voltage is normalized to $hf/2e$, and shows a clear Shapiro response.

sition, indicating that the critical current of the junction in this state is suppressed to below the measurement current. This difference in I_c between the two states allows us to read out the magnetic state of the memory element electrically. To unambiguously demonstrate the superconducting proximity effect in our devices, we show the appearance of Shapiro steps in the IV-characteristic of device A under the application of RF radiation, which is supplied by a nearby antenna. We carry out these measurements at 1.6 K in the V-state. The step height in the IV-characteristic shown in Figure 5.2b is in units $hf/2e$ (where h is the Planck constant, f is the frequency of the RF radiation, and e the electron charge), confirming the Shapiro response.

5.3. CONTROLLABLE SWITCHING

To show the bistability of the spin textures, we examine the dependence of I_c on the in-plane 'writing' fields H_x and H_y along the long and the short axis of the ellipse, respectively. The results are shown in Figure 5.3a,b, accompanied by the simulated spin textures in Figure 5.4. If the sample is in the M-state ("0"), I_c is 5 μA. The datum "1" can be written by increasing the field along the short axis of the ellipse. At a field of 40 mT, I_c grows to above 20 μA, which is accompanied by a buckling of the simulated spin texture. Upon decreasing the field to zero, the high I_c state is retained, and the buckled spin texture evolves into two vortices. Therefore, the device is converted into the V-state ("1"). Conversely, the M-state can be written in the device by applying a field parallel to the long axis of the ellipse. The field effectively displaces the vortices towards the edges of the sample. At a field of 15 mT, they are fully pushed out from the ellipse, and the spins align in the M-state. This is accompanied by a drop in I_c back to 5 μA. The low I_c is stable upon decreasing the field back to zero in the M-state.

Figure 5.3c,d show the total energy associated with the simulated spin texture as a function of externally applied field (i.e., the sum of the exchange, demagnetization, and Zeeman energies). Two branches can be discerned corresponding to the two states, both stable at zero field. In the simulations, the buckled state, which is required for the stabilization of the V-state state, appears above 45 mT. During the converse switching operation, a field of 25 mT is required to magnetize the ellipse. Remarkably, we find that both fields closely follow the experimental values with only a slight offset, which can be attributed to the reduced geometry of the contacts and the finite field steps used in the simulations.

We examine the performance of our devices by repeatably switching them between the two states while studying the transport behavior. Figure 5.5a shows the zero-field IV-characteristic of the two states. Based on the difference in I_c, we can define a readout current corresponding to a finite voltage in the M-state, but a zero voltage in the V-state. We cycle the device between the two states (using a 40 mT field) and acquire the voltage at the readout current in each state. In Figure 5.5b, we show a histogram

of the measured voltage at a readout current of 30 µA, totaling 78 subsequent writing cycles. There is no overlap in the histogram, making the states highly distinguishable. Since the readout current density is far too low to alter the spin texture, the readout operation is fully non-destructive. Furthermore, by heating the ellipse to above the T_c of the superconducting layer between subsequent write and read operations, we confirm the non-volatility of its memory. This holds even when the sample is warmed to room temperature and stored for days. Additionally, to test the resilience to perturbations of the spin texture, we try to cycle between the states using a field of 10 mT. We find these fields insufficient to alter I_c, demonstrating the stability of our devices.

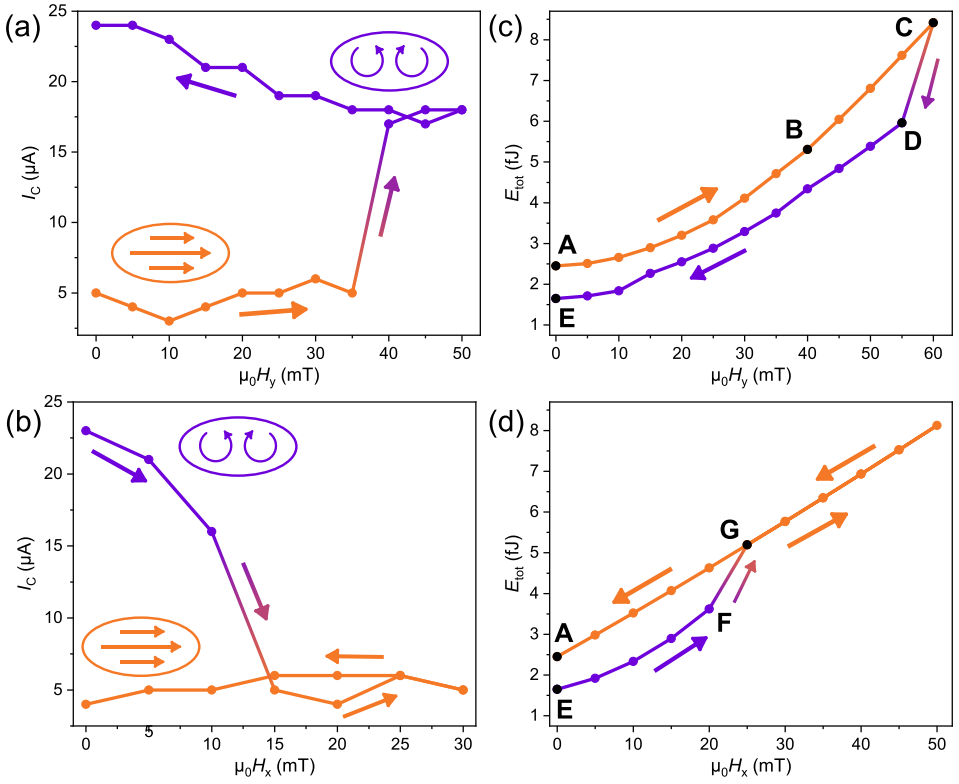

Figure 5.3: The critical current I_c, the total simulated energy E_{tot} and the spin texture of the device as a function of H_x (field along the long axis), and H_y (along the short axis). Results obtained on device B at 1.7 K. (a) and (b) depict $I_c(H_y)$ and $I_c(H_x)$. In (a), the field is increased along the short axis of the ellipse. At 40 mT I_c increases sharply, effectively transforming the M-state into the V-state. The reverse operation is shown in (b): by increasing the field - parallel to the long axis of the ellipse - to 15 mT, the critical current drops to 5 µA, bringing the device back to the M-state. (c) and (d) show E_{tot} corresponding to the in-plane field sweeps. Two branches can be seen in both panels, corresponding to the V- and M-state. A change of magnetic state coincides with a jump from one branch to the other. We can predict the switching fields correctly within a small error. Snapshots of the spin texture during the simulations in (c) and (d) are shown in Figure 5.4. These data points are colored black in (c) and (d) and labeled with boldface letters accordingly.

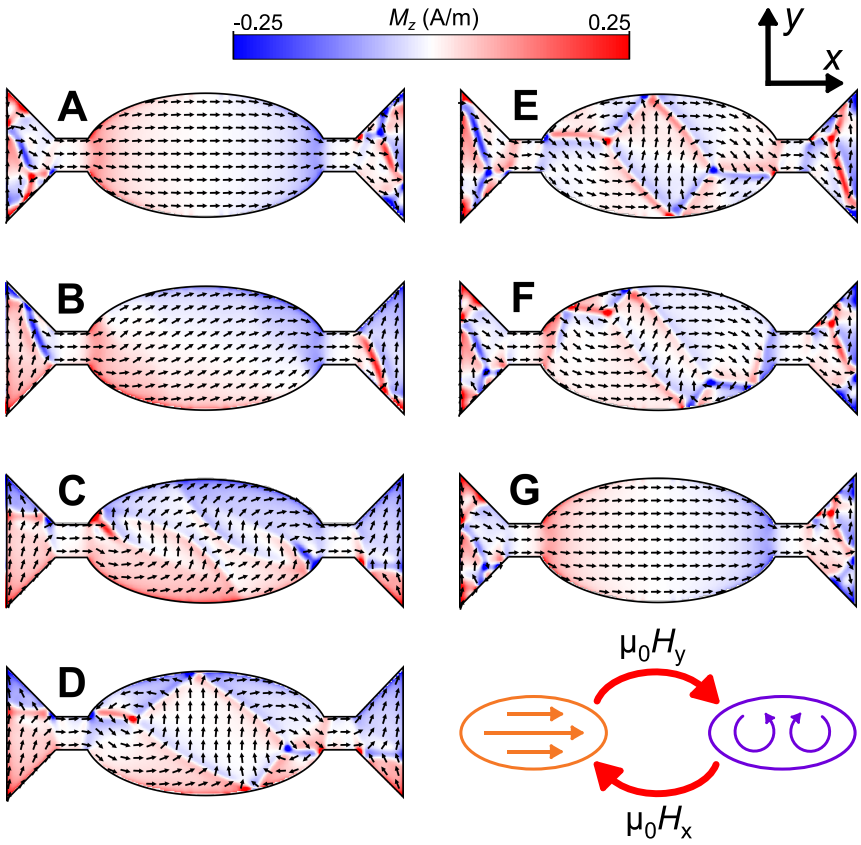

Figure 5.4: Snapshots of the spin texture during the simulated field sweeps presented in Figure 5.3. Here the color scale indicates the magnetization of the top of the Co-layer and the boldface letters correspond to the ones in Figure 5.3c,d.

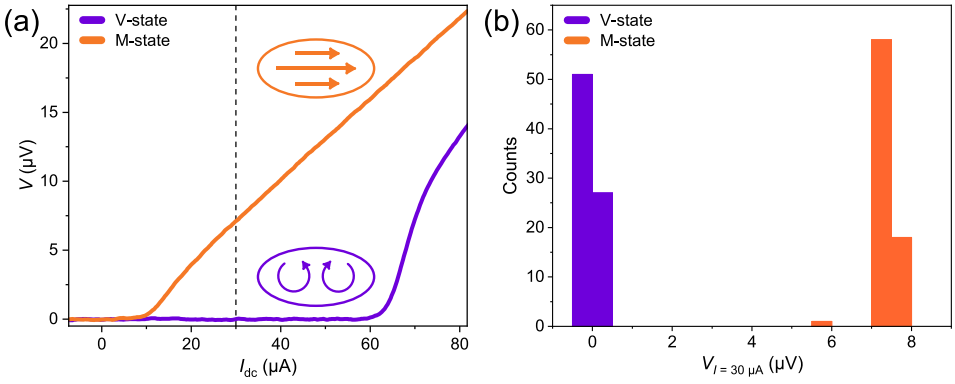

Figure 5.5: Fidelity of the writing cycles of device A. The IV-characteristics of the two states, measured at 1.6 K, are shown in (a). Based on these curves, we define a readout current corresponding to a finite voltage in the M-state and zero voltage in the V-state. We cycle the device between the two states 78 times and measure the voltage before each subsequent switch. (b) shows a histogram of the readout voltages, measured using a 30 μA current (the dotted line in (a)).

5.4. STRAY FIELD DRIVEN MECHANISM

We now discuss the mechanism used for suppressing the I_c in the M-state, based on the local stray field emerging from the ferromagnet. To illustrate this, we obtain the $I_c(B)$-pattern for Junction B. Note that the magnitude of the out-of-plane fields is insufficient to alter the global spin texture of the device (i.e., the out-of-plane fields cannot transform the M-state to the V-state or vice versa). We present such measurements, obtained on sample B, for the V-state and the left and right magnetized M-state in the color maps of Figure 5.6a-c. For this sample, we observe a pattern with a single middle lobe and heavily suppressed side lobes. Samples with higher I_c values show a Fraunhofer-like interference pattern, indicating a uniform distribution of I_c throughout the weak link, as can be seen in Appendix B, where we present additional interference patterns. The pattern is centered at zero field for the V-state (Figure 5.6c). By

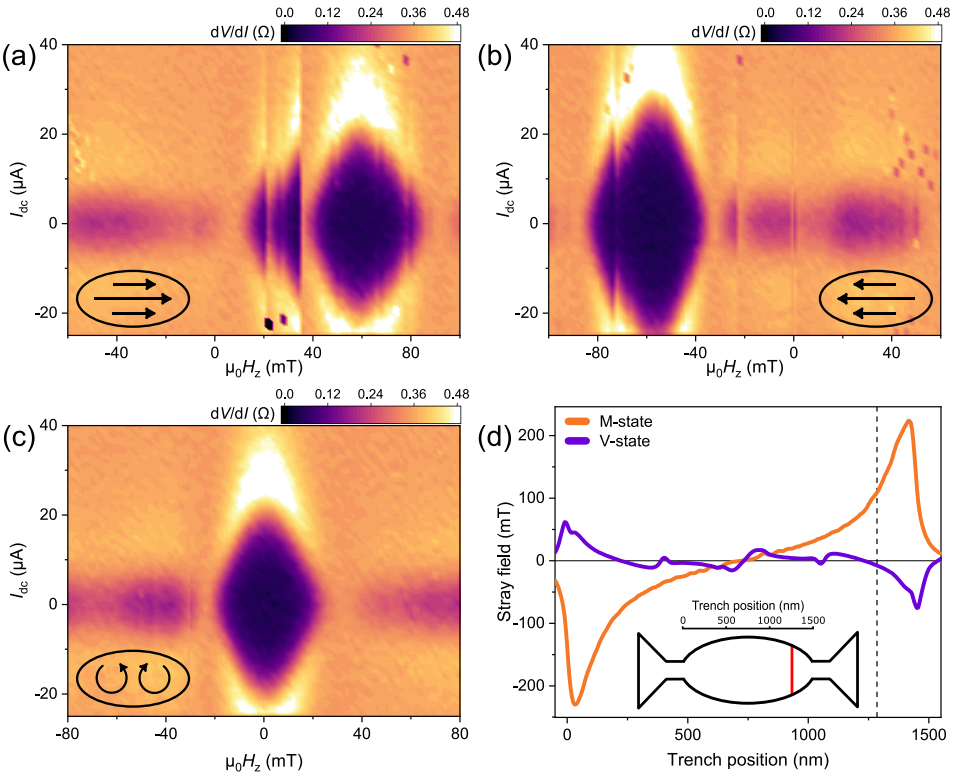

Figure 5.6: Stray fields cause a shift in I_c. (a) to (c) respectively show the superconducting interference patterns in the right magnetized M-state, left magnetized M-state, and the V-state obtained on device B. Although the shape of the $I_c(B)$-pattern does not change, the middle lobe of the pattern is shifted in the V-state with respect to the pattern in the M-state (for both magnetizations). Some measurement glitches are visible in (a) and (b): these result from sudden small magnetic configurations in the sample. Stray fields from the ferromagnetic layer cause the shift, as is demonstrated in (d): the simulated field shift for different trench locations. The vertical line in (d) corresponds to the actual location of the trench (see Figure 5.1). The inset shows the geometry of the sample with the corresponding scale distribution. The red line indicates the actual location of the trench.

switching to either of the M-states (Figure 5.6a,b), the shape of the $I_c(B)$-pattern is not altered, yet shifted by around 60 mT from zero applied field. Moreover, the magnetization direction in the M-state determines the sign of this shift. Therefore, it is evident that the suppressed I_c of the M-state is a result of the local stray fields from the Co layer, introducing a shift in the $I_c(B)$-pattern. However, what makes our spin-textured devices truly stand out from previous Josephson memory elements, is that we use a writing field (40 mT) that is noticeably smaller than the resulting shift (60 mT).

In the following, we describe how the pattern shift can be quantified by simulating the stray flux entering the junction. We sum the z-component of the flux - evaluated in a thin sheet above the Cobalt layer - over an integration window to obtain the local stray fields threading area of the window. The size of this window is chosen to reflect the trench area, yielding an estimate of the stray fields penetrating the junction. Figure 5.6d displays the simulated (stray field-induced) pattern shift as a function of the window location; the vertical line indicates the location of the trench in the actual sample. This shows that the V-state corresponds to negligible stray fields penetrating the junction, accounting for the symmetric pattern in Figure 5.6c lacking horizontal offset. The M-state corresponds to an 80 mT shift, which closely follows the 60 mT offset in the $I_c(B)$-patterns. Note that the simulated stray field is symmetric with respect to the center of the sample. This reflects the sign change that occurs when the magnetization direction is reversed.

Note that the spin texture snapshots of Figure 5.4 show the source of the stray fields. In the M-state, the ellipse features a dipole-like field along its long axis, which is absent in the V-state. We do observe some stray fields in the V-state, although these average out over the junction area. Therefore the total shift in the $I_c(B)$-pattern remains zero. During the field sweep along the short axis of the ellipse (i.e., switch from M-state to V-state), the spin texture buckles before two vortices stabilize, as can be seen in the snapshots **B** and **C** in Figure 5.4. When this buckling occurs, the dipole-like field no longer points along the long axis of the ellipse, and consequently, the stray fields average out over the junction area. This explains why the high I_c state occurs before two vortices enter the ellipse.

5.5. PAIRING SYMMETRY OF THE SUPERCURRENTS

In Chapter 4, we found spin texture to be a prerequisite for the superconducting proximity effect, which led to the conclusion that the transport in the disk-shaped S−F−S junctions is dominated by long-range triplet (LRT) Cooper pairs. In this case, however, we cannot be certain about the LRT scenario. Due to the similarity to the circular devices, LRT correlations can be expected in the V-state of the ellipse-shaped devices described here. However, there are several inconsistencies; the most notable ones are discussed here. First, contrary to the disk-shaped devices, removing the spin texture

from our junctions does not suppress the proximity effect, i.e., the maximum of $I_c(B)$ for both the M- and V-states are quite similar. Secondly, while the $I_c(B)$-patterns of the disk-shaped devices are highly sensitive to the subtle changes in the spin texture, the elliptic junctions show the same type of pattern for widely different magnetic states. These observations seem to counter the notion of the LRT correlations and indicate that transport in the elliptic junctions is carried by the short-range triplet correlations instead. However, one could argue that even the M-state still features some spin texture near the edges of the sample (due to the narrow tapered shape of the ellipse; see Figure 5.1b), which possibly allows for the generation of LRT correlations. Finally, the similar $I_c(B)$-patterns between the magnetic states can possibly be caused by the relatively short junction width. Indeed, the length of the trench in the disk-shaped devices is typically between 1 μm and 1.6 μm, whereas the trench length of the ellipse devices presented here is less than 600 nm; the current channels might therefore overlap sufficiently to produce a single channel interference pattern. At this stage, no conclusions can be drawn on the triplet or singlet nature of the supercurrents in the elliptical devices, and further experiments are necessary. We emphasize, however, that the mechanism for the shift in the $I_c(B)$-patterns (i.e., the stray fields) holds for both singlet and triplet pairing symmetries.

5

5.6. CONCLUSION AND OUTLOOK

We demonstrate the realization of a non-volatile superconducting memory element based on magnetic textures in an S−F−S Josephson junction. The ellipsoidal shape of the device leads to two stable magnetic states at zero applied magnetic field: a fully magnetized state and a state containing ferromagnetic vortices. These can be associated with the data "0" and "1", respectively. By applying and removing an externally applied in-plane field, we can reliably switch between these states, performing a write operation. We find a strong suppression of the critical current in the magnetized state, which allows for a non-destructive determination of the spin state, and therefore, electrical readout of the bit. By combining transport experiments and micromagnetic simulations, we show that the difference in critical current between the two states results from internal stray fields originating from the ferromagnetic layer of the device, which creates a local offset field in the junction. Since the ferromagnetic textures can be controllably manipulated with RF radiation, storing information in mesoscopic S−F devices can provide an exciting avenue for realizing ultra-fast electronics. Besides, strain-mediated switching of similar elliptical devices has been recently theoretically studied and shown to be a good alternative to switching using externally applied fields[28]. Combined with the possibility of long-range triplet supercurrents in hybrid devices, the memory devices presented here can form an essential building block for superconducting spintronics.

APPENDICES

A. MICROMAGNETIC SIMULATIONS

The micromagnetic simulations on the elliptical samples are performed using the GPU-based MuMax^3 program[29]. The cobalt layer is divided into a mesh of 5 nm cubic cells. The exchange coefficient is set to 3×10^{-11} J/m, and the saturation magnetization is 1.4×10^{-6} A/m. We choose the Gilbert damping constant to be 0.5, to allow for faster convergence and therefore increased computation speed. As the cobalt film is polycrystalline due to the Ar-sputtering method, we use a zero anisotropy constant. The micromagnetic simulations of the disk devices presented in the previous chapter are carried out within the Object Oriented MicroMagnetic Framework (OOMMF) simulation software. A full description of these simulations is reported elsewhere, although the parameters used are identical to those described here[30]. The only difference lies in the calculation method: OOMMF is CPU-based, whereas MuMax^3 is GPU-based.

We have included vacuum cells around the magnetic structure in all our simulations. These feature no spin, yet magnetic fields can penetrate them. Therefore, in each steady-state solution, we gain full insight into the stray fields around the magnetic layer. In order to calculate the stray fields penetrating the junction, we sum the z-component of these stray fields directly above the magnetic layer (i.e., penetrating the superconducting layer perpendicular to the charge transport direction). We define a window of area A and find the field penetrating this window by dividing the flux Φ by its area. The total flux is given by the sum of the flux in each cell, which is determined by the product of the z-component of the field penetrating the cell and the cell area. Since each cell has the same area by design, this leads to:

$$\Delta B = \frac{\Phi}{A} = \frac{1}{A} \sum B_{z,\mathrm{i}}\, A_{\mathrm{cell,i}} = \frac{1}{N_{\mathrm{cells}}} \sum B_{z,\mathrm{i}} \tag{5.1}$$

Here we recognize that the total field penetrating the window equals the average field per cell, which can be evaluated from the simulation results.

Ideally, the area of the integration window is chosen to reflect the effective area of the junction. However, in Chapter 3, we found that devices of these dimensions are in the non-local limit. The effective area is therefore determined by the geometry and not by λ_{L}. Moreover, although we provide a method for calculating the magnitude of the effective area in Chapter 3, we cannot specify the geometry of this area. Besides, due to the taped shape of the ellipse, using the calculated effective area and assuming a rectangular junction area would lead to incorrectly accounting for fields outside the sample geometry. More importantly, evaluating the effective area would require a separate calculation for each junction position, a process that is, as of now, not automatized (i.e., for every geometry, the Neumann boundary conditions are found by hand).

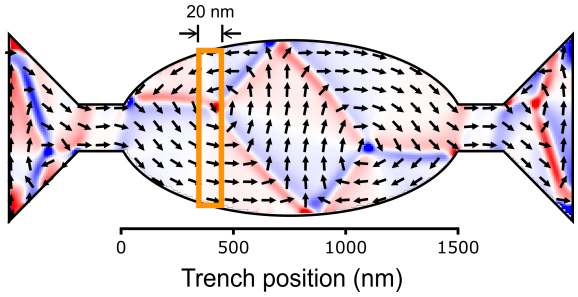

Figure A.1: Graphical representation of the integration window, used to calculate the local stray fields (in orange). The integration window is chosen to reflect the size of the physical junction. The width equals that of the trench (20 nm), and the length is equal to the local width of the ellipse. By positioning the integration window at different locations (i.e., trench positions), we can evaluate the stray fields at different locations along the ellipse. The axis labeled 'Trench position' coincides with the x-axis of Figure 5d of the main text.

We also assumed symmetric superconducting electrodes in our calculations presented in Chapter 3. When the trench is not centered, the superconducting electrodes are not symmetric, complicating the calculations. In order to solve these issues, we specify a rectangular window with a fixed width (set by the junction width: 20 nm) and a variable length. We match the length of the window to that of the local width of the ellipse. By this choice, we minimize the summation of the field outside the device geometry. By varying the location of the center of the integration window, we evaluate an expression of the stray fields that locally penetrate the superconductor. A graphical representation of the integration window is shown in Figure A.1.

B. ADDITIONAL DATA

In this chapter, we provide results on two different devices, named A and B. In this Appendix, we provide additional data obtained on these samples. Supporting Figure B.1 shows the in-plane field sweeps obtained on device A. Similar to device B, there is a transition from the M-state to the V-state at 40 mT when increasing the field along the short axis of the ellipse. This is accompanied by an increase in critical current, which is retained upon reducing the field to zero. The converse operation is carried out by applying the field along the long axis of the ellipse. We find that 5 mT is sufficient to reduce the critical current to the value corresponding to the M-state. This is lower than the corresponding field for device B (15 mT). Figure B.2 shows the typical IV-characteristics of the V-state and M-state for device B. A clear voltage difference is measured at a readout current of, for example, 15 μA. No histogram was obtained on this device. Finally, we present a full dataset obtained on a third device in Figures B.3,B.4 and, B.5, named device C.

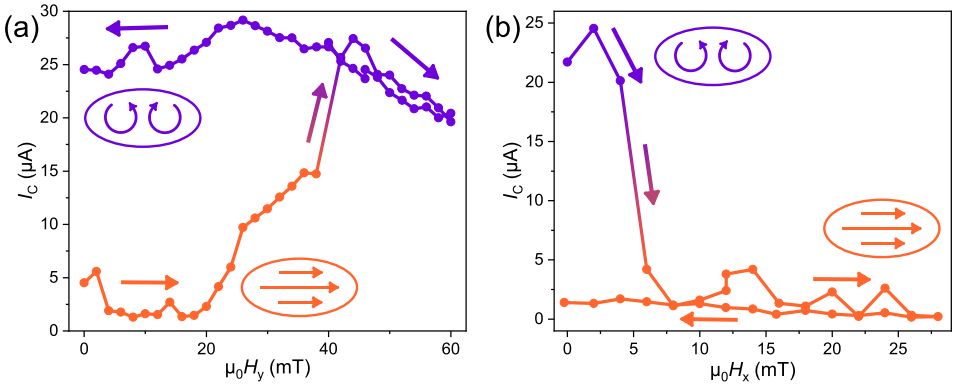

Figure B.1: The critical current I_c as a function of H$_x$ (field along the long axis), and H_y (field along the short axis). Similar data as presented in Figure 5.3 of the main text, obtained on device A at 1.7 K. (a) and (b) depict $I_c(H_y)$ and $I_c(H_x)$ respectively. In (a) the field is increased along the short axis of the ellipse. Like sample B, at 40 mT I_c increases sharply, effectively transforming the M-state into the V-state. By increasing the field parallel to the long axis of the ellipse (shown in (b)), the critical current drops to the low I_c state at 5 mT. This is lower than the 15 mT, needed to switch device B.

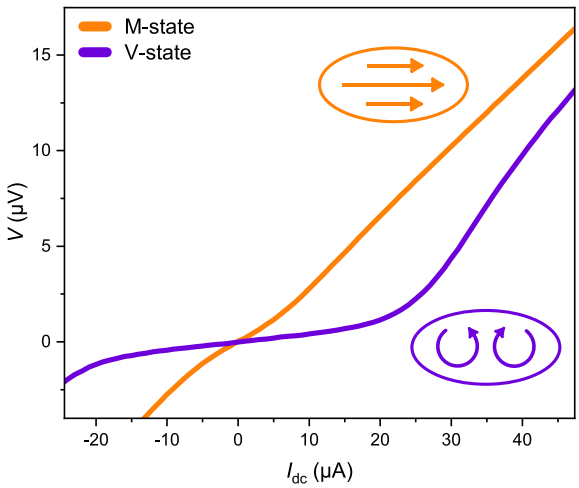

Figure B.2: The typical IV for both states in device B. By choosing a proper read-out current (e.g. 15 μA), a clear voltage difference between the two states can be measured.

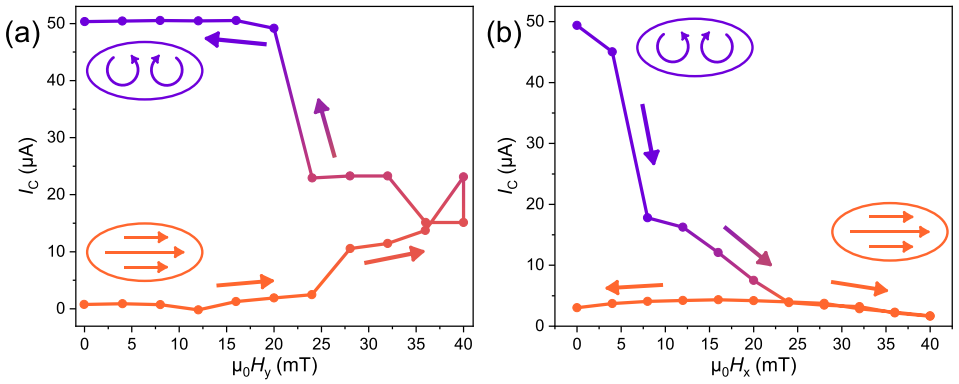

Figure B.3: The critical current I_c as function of H_y (field along the short axis, shown in (a)), and H_x (field along the long axis, shown in (b)). Similar data as presented in Figure 3 of the main text, obtained on a third device, called device C. Data acquired at 2 K. In (a), the field is increased along the short axis of the ellipse; by increasing the field to 40 mT, the spin texture is buckled and upon reducing the field to zero, the V-state and entailing high I_c state is retrieved. By increasing the field parallel to the long axis of the ellipse, the critical current drops to the low I_c state corresponding to the M-state.

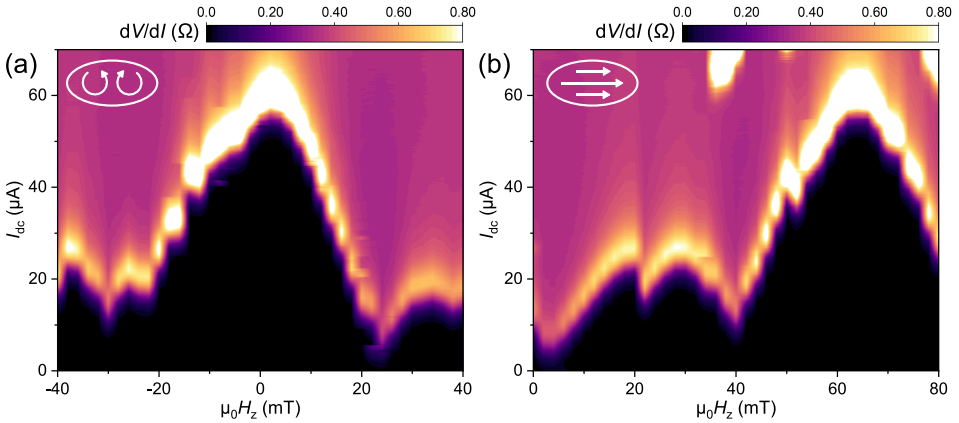

Figure B.4: (a) to (b) respectively show the $I_c(B)$-patterns in the V-state and the M-state in a third device, named device C. Although the shape of the $I_c(B)$-pattern does not change, the center lobe of the pattern is shifted in the V-state with respect to the pattern in the M-state. This is the same behavior as observed for device B (presented in the main text).

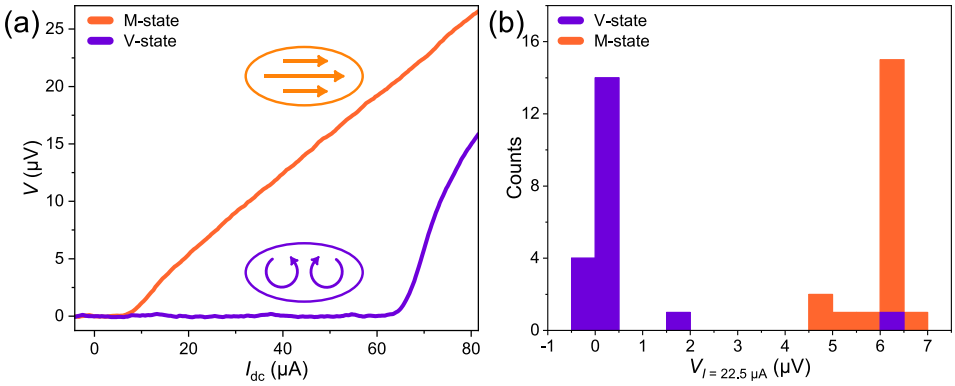

Figure B.5: Fidelity of writing cycles in a third device, named device C. In (a) we show the IV-characteristic for both states. We define a read-out current of 22.5 μA. We cycle the device between the states 20 times and record the voltage at the read-out current. (b) shows a histogram of these voltages.

REFERENCES

[1] Andrae, A. & Edler, T. On Global Electricity Usage of Communication Technology: Trends to 2030. *Challenges* **6**, 117–157 (2015).

[2] Jones, N. How to stop data centres from gobbling up the world's electricity. *Nature* **561**, 163–166 (2018).

[3] Holmes, D. S., Ripple, A. L. & Manheimer, M. A. Energy-Efficient Superconducting Computing—Power Budgets and Requirements. *IEEE Trans. Appl. Supercond.* **23**, 1701610–1701610 (2013).

[4] Soloviev, I. I. *et al.* Beyond Moore's technologies: Operation principles of a superconductor alternative. *Beilstein J. Nanotechnol.* **8**, 2689–2710 (2017).

[5] Chen, L. *et al.* Miniaturization of the superconducting memory cell via a three-dimensional Nb nano-superconducting quantum interference device. *ACS Nano* **14**, 11002–11008 (2020).

[6] Butters, B. A. *et al.* A scalable superconducting nanowire memory cell and preliminary array test. *Supercond. Sci. Technol.* **34**, 035003 (2021).

[7] Hilgenkamp, H. Josephson Memories. *J. Supercond. Nov. Magn.* **34**, 1621–1625 (2021).

[8] Larkin, T. I. *et al.* Ferromagnetic Josephson switching device with high characteristic voltage. *Appl. Phys. Lett.* **100**, 222601 (2012).

[9] Vernik, I. V. *et al.* Magnetic Josephson junctions with superconducting interlayer for cryogenic memory. *IEEE Trans. Appl. Supercond.* **23**, 1701208 (2013).

[10] Caruso, R. *et al.* RF assisted switching in magnetic Josephson junctions. *J. Appl. Phys.* **123**, 133901 (2018).

[11] Caruso, R. *et al.* Properties of ferromagnetic Josephson junctions for memory applications. *IEEE Trans. Appl. Supercond.* **28**, 1800606 (2018).

[12] Baek, B., Rippard, W. H., Benz, S. P., Russek, S. E. & Dresselhaus, P. D. Hybrid superconducting-magnetic memory device using competing order parameters. *Nat. Commun.* **5**, 3888 (2014).

[13] Golod, T., Iovan, A. & Krasnov, V. M. Single Abrikosov vortices as quantized information bits. *Nat. Commun.* **6**, 8628 (2015).

[14] Dayton, I. M. *et al.* Experimental demonstration of a Josephson magnetic memory cell with a programmable π-junction. *IEEE Magn. Lett.* **9** (2018).

[15] Nevirkovets, I. P. & Mukhanov, O. A. Memory cell for high-density arrays based on a multiterminal superconducting-ferromagnetic device. *Phys. Rev. Applied* **10**, 034013 (2018).

[16] Niedzielski, B. M. *et al.* Spin-valve Josephson junctions for cryogenic memory. *Phys. Rev. B* **97**, 024517 (2018).

[17] Madden, A. E., Willard, J. C., Loloee, R. & Birge, N. O. Phase controllable Josephson junctions for cryogenic memory. *Supercond. Sci. Technol.* **32**, 015001 (2018).

[18] Satchell, N. *et al.* Spin-valve Josephson junctions with perpendicular magnetic anisotropy for cryogenic memory. *Appl. Phys. Lett.* **116**, 022601 (2020).

[19] Martinez, W. M., Pratt, W. P. & Birge, N. O. Amplitude Control of the Spin-Triplet Supercurrent in S/F/S Josephson Junctions. *Phys. Rev. Lett.* **116**, 1–5 (2016).

[20] Glick, J. A. *et al.* Phase control in a spin-triplet SQUID. *Sci. Adv.* **4**, 1–8 (2018).

[21] de Andrés Prada, R. *et al.* Memory-functionality superconductor/ferromagnet/superconductor junctions based on the high-T_c cuprate superconductors $YBa_2Cu_3O_{7-x}$ and the colossal magnetoresistive manganite ferromagnets $La_{2/3}X_{1/3}MnO_{3+\delta}$(X=Ca,Sr). *Phys. Rev. B* **99**, 214510 (2019).

[22] Weigand, M. *et al.* Vortex core switching by coherent excitation with single in-plane magnetic field pulses. *Phys. Rev. Lett.* **102**, 077201 (2009).

[23] Uhlíř, V. *et al.* Dynamic switching of the spin circulation in tapered magnetic nanodisks. *Nat. Nanotechnol.* **8**, 341–346 (2013).

[24] Kammerer, M. *et al.* Magnetic vortex core reversal by excitation of spin waves. *Nat. Commun.* **2**, 279 (2011).

[25] Linder, J. & Robinson, J. W. A. Superconducting spintronics. *Nat Phys* **11**, 307–315 (2015).

[26] Eschrig, M. & Löfwander, T. Triplet supercurrents in clean and disordered half-metallic ferromagnets. *Nat. Phys.* **4**, 138–143 (2008).

[27] Yang, G., Ciccarelli, C. & Robinson, J. W. A. Boosting spintronics with superconductivity. *APL Mater.* **9**, 050703 (2021).

[28] Song, X. *et al.* Strain-mediated voltage-controlled magnetic double-vortex states in elliptical nanostructures. *J. Magn. Magn. Mater.* **547**, 168729 (2022).

[29] Vansteenkiste, A. *et al.* The design and verification of MuMax3. *AIP Adv.* **4**, 107133 (2014).

[30] Lahabi, K. *et al.* Controlling supercurrents and their spatial distribution in ferromagnets. *Nat. Commun.* **8**, 2056 (2017).